

SERVICE DE MÉCANIQUE STATISTIQUE ET SYSTÈMES
COMPLEXES

PHYS-F435

Quantum Hall effect



Student :
JAMOTTE MAXIME

Supervisors :
DR MARCO DI LIBERTO
DR NATHAN GOLDMAN

Academic year 2018-2019

Abstract

This report is the the conclusion of an intership in the *Service de Mécanique Statistique et Systèmes Complexes de l'Université Libre de Bruxelles*. The main goal of this internship is to get an insight of topological physics. The basic notions of topological physics are introduced and applied to different models. The integer quantum Hall effect is highlighted through the $1/3$ Harper-Hofstadter model. We end up with a comparison to literature. All the figures and results have been obtained thanks to the codes attached to this document gathered in the .zip file *JAMOTTE_Maxime_PHYSF435.zip*.

Contents

1	Introduction	2
1.1	Hall effects	2
1.2	Adiabatic theorem	3
1.3	Geometrical phase	3
1.4	Change of gauge	4
1.5	Chern numbers	5
1.6	Fukui-Hatsugai-Suzuki and Niu methods	5
2	Dirac and Honeycomb models	6
2.1	Dirac model	6
2.2	Honeycomb model	7
3	Harper-Hofstadter model ($\phi = 1/3$)	9
3.1	Bloch states and magnetic Brillouin zone	11
3.2	Toroidal boundary conditions	13
3.3	Cylindrical boundary conditions	15
3.4	Open boundary conditions	18
4	Dynamics	19
4.1	Comparison of velocities between cylindrical and open boundary systems	21
4.2	Paper on photonics experiments	21
5	Conclusions	25

1 Introduction

Let's first explain what the quantum Hall effect is and what are the key notions to understand it. We also present two methods to compute quantities of interest.

1.1 Hall effects

In classical mechanics, when an electric field is applied on the ends of a conductive material, let's say in the x direction, a current J_x , parallel to E_x , is produced. If the material is immersed in a magnetic field, the moving electrons progressively deviate from a straight trajectory in a perpendicular plan respectively to the applied magnetic field. In a finite size material with adequate dimensions, this deviation can cause an accumulation of negative charges on one side of the material and an accumulation of positive charges on the opposite one. This leads to induce an electric field between the opposed charges zones – see figure 1 – called the Hall electric field E_H , that is related to J_x by the Ohm's law $\mathbf{J} = \boldsymbol{\sigma} \mathbf{E}_H$, with $\boldsymbol{\sigma}$ the conductivity tensor. Since the current in the x direction induces a electric field in the y direction, we conclude that the element σ_{yx} is don't vanish.

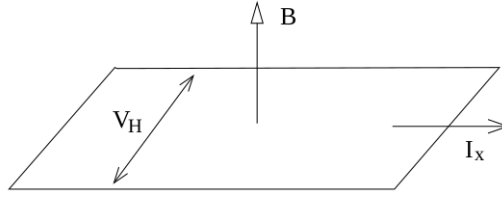


Figure 1: Image from the reference [1]. Classical Hall effect. V_H is the electric potential due to E_H .

The integer quantum Hall effect on the other hand is historically the first phenomenon where momentum-space topology was recognized to lead to observable physical phenomenon. To experiment a such effect, schematically, we can apply an electric field between two opposite edges of an insulator and expect to measure a current between the two other edges since the Ohm law still holds. We will face a quantization of the conductivity:

$$\sigma_{yx} = \frac{e^2}{h} n \quad n \in \mathbb{Z} \quad (1.1)$$

where e is the charge of the electron and h is the Planck constant. The dependence of σ_{yx} in the magnetic field then takes the form of trays and switch from n to $n + 1$ for a determined value of \mathbf{B} . As we will see, the current actually propagates along the edges, not through the bulk (since we face an insulator).

1.2 Adiabatic theorem

Let be an Hamiltonian H depending on an exterior parameter¹ λ evolving in parameter space with given dimension [2] [3][4] [5]. Let's suppose that λ vary and comes back to its initial value after a time T : $\lambda(0) = \lambda(T)$. If we denote eigenvalues and eigenvectors of $H(\lambda)$ respectively $E_n(V)$ and $|\psi_n(\lambda)\rangle$, $n \in \mathbb{N}$ such that

$$H(\lambda) |\psi_n(\lambda)\rangle = E_n(\lambda) |\psi_n(\lambda)\rangle.$$

We impose in addition that the eigenvectors basis remain orthonormal, regardless the value of λ . Let's have a look at the evolution in time of the vector

$$|\psi(t)\rangle = \sum_n c_n(t) |\psi[\lambda(t)]\rangle. \quad (1.2)$$

If we report this expression into the Schrödinger equation,

$$i\hbar \frac{d|\psi\rangle}{dt} = \hat{H}[\lambda] |\psi(t)\rangle, \quad (1.3)$$

and by multiplying by $\langle\psi_\ell[\lambda(t)]|$, we get

$$i\hbar \dot{c}_\ell = E_\ell(t) c_\ell(t) - \hbar \sum_n \alpha_{\ell,n}(t) c_n(t), \quad (1.4)$$

where

$$\alpha_{\ell,n}(t) = i\dot{\lambda} \cdot \langle\psi_\ell(\lambda)|\nabla\psi_n(\lambda)\rangle = \frac{1}{i\hbar\omega_{\ell,n}} \langle\psi_\ell|\frac{d\hat{H}}{dt}|\psi_n\rangle. \quad (1.5)$$

We defined $\hbar\omega_{\ell,n} = E_\ell[\lambda(t)] - E_n[\lambda(t)]$. For the rest of this discussion, we impose two things: the eigenvalues are non-degenerated and λ evolves slowly in time, i.e.

$$n \neq \ell : \quad \frac{|\alpha_{\ell,n}^{\max}|}{|\omega_{\ell,n}^{\min}|} = \frac{\text{maximum angular velocity of } \psi_n}{\text{minimum Bohr pulsation of } \psi_n} \ll 1 \quad (1.6)$$

This condition ensures that the probability of ψ_ℓ remain at the same energy stays all along near 1: $|c_\ell(t)| \simeq 1$. The last thing we need to study is the phase of this coefficient $c_\ell(t)$.

1.3 Geometrical phase

We consider a quantum system for which the adiabatic approximation is valid. At $t = 0$, the system is in an eigenstate ψ_ℓ of the Hamiltonian $\hat{H}[\lambda(0)]$ et we suppose that it is so at every moment:

$$|\psi(t)\rangle = \sum_n c_n(t) |\psi_n[\lambda(t)]\rangle \simeq c_\ell(t) |\psi_\ell[\lambda(t)]\rangle. \quad (1.7)$$

By substituting this state in the Schrödinger equation, we get

¹This parameter could be a magnetic field or quasimomenta $\mathbf{k} = \frac{2\pi i}{\lambda}$, for λ a wavelength.

$$i\hbar\dot{c}_\ell = \left[E_\ell(t) - i\hbar\dot{\boldsymbol{\lambda}} \cdot \mathcal{A}_\ell(\boldsymbol{\lambda}) \right] c_\ell, \quad (1.8)$$

with $\mathcal{A}_\ell(\boldsymbol{\lambda}) = -i \langle \psi_\ell | \nabla_{\boldsymbol{\lambda}} | \psi_\ell \rangle$ is the *Berry connection*. Hence, we find

$$c_\ell = c_\ell(0) \exp \left\{ \underbrace{-\frac{i}{\hbar} \int_0^t E_\ell(t') dt'}_{i\Phi^{\text{dyn.}}} + \underbrace{\frac{i}{\hbar} \int_{\boldsymbol{\lambda}(0)}^{\boldsymbol{\lambda}(t)} \mathcal{A}_\ell(\boldsymbol{\lambda}) d\boldsymbol{\lambda}}_{i\Phi^{\text{geom.}}} \right\} \quad (1.9)$$

with $d\boldsymbol{\lambda} = \dot{\boldsymbol{\lambda}} dt$. We notice that the dynamical phase $\Phi^{\text{dyn.}}$ doesn't depend on the followed path during the evolution but on its duration, in contrast to the geometrical phase $\Phi^{\text{geom.}}$ that does depend only on the followed path $\boldsymbol{\lambda}(t)$. We note that this path can be closed, that is $\boldsymbol{\lambda}(0) = \boldsymbol{\lambda}(T)$ for T the time needed to close the path:

$$\Phi^{\text{geom.}} = \frac{1}{\hbar} \oint_{\mathcal{C}} \mathcal{A}_\ell(\boldsymbol{\lambda}) d\boldsymbol{\lambda} \quad (1.10)$$

If the parameters space is 3-dimensional and if the hypothesis of the Stokes' theorem² are satisfied, we have

$$\Phi^{\text{geom.}} = \frac{1}{\hbar} \iint_{\mathcal{S}} \boldsymbol{\Omega}_\ell \cdot d^2\mathcal{S}, \quad (1.11)$$

where we introduced the *Berry curvature*

$$\boldsymbol{\Omega}_\ell = \nabla_{\boldsymbol{\lambda}} \wedge \mathbf{A}_\ell = -i \nabla_{\boldsymbol{\lambda}} \wedge \langle \psi_\ell | \nabla_{\boldsymbol{\lambda}} | \psi_\ell \rangle = -i \langle \nabla_{\boldsymbol{\lambda}} \psi_\ell | \wedge | \nabla_{\boldsymbol{\lambda}} \psi_\ell \rangle \quad (1.12)$$

and defined \mathcal{S} as the surface relying on the curve \mathcal{C} .

1.4 Change of gauge

Let's have a look at the consequences of a $U(1)$ gauge change on the Berry connection and the Berry curvature. To do this, we multiply the state $|\psi_\ell[\boldsymbol{\lambda}]\rangle$ by a phase factor $\chi_\ell[\boldsymbol{\lambda}]$:

$$|\psi_\ell[\boldsymbol{\lambda}]\rangle \rightarrow e^{i\chi_\ell[\boldsymbol{\lambda}]} |\psi_\ell[\boldsymbol{\lambda}]\rangle \quad (1.13)$$

If the function $\chi_\ell[\boldsymbol{\lambda}]$ is sufficiently regular at every point, the Berry connection must transform as

$$\mathcal{A}_\ell(\boldsymbol{\lambda}) \rightarrow \tilde{\mathcal{A}}_\ell(\boldsymbol{\lambda}) = \mathcal{A}_\ell(\boldsymbol{\lambda}) - \nabla \chi_\ell[\boldsymbol{\lambda}] \quad (1.14)$$

to let the problem gauge invariant. Thus, the Berry curvature and the Berry phase stay unchanged

²In particular, the parameters space must be simply connected.

since the rotational of a gradient vanishes on a closed path, as the integral of a gradient³. We can then deduce that $e^{i\Phi_{\text{geom}}} = e^{i\tilde{\Phi}_{\text{geom}}}$. This implies the Berry curvature is gauge invariant.

1.5 Chern numbers

From now on, the parameters space will be the quasi-momenta space and we will restrict ourselves to the Brillouin zone. The Berry curvature is then

$$\Omega_{\mathbf{k}} = i \left(\langle \partial_{k_x} u_{\mathbf{k}} | \partial_{k_y} u_{\mathbf{k}} \rangle - \langle \partial_{k_y} u_{\mathbf{k}} | \partial_{k_x} u_{\mathbf{k}} \rangle \right) \cdot \mathbf{u}_z \quad \in \mathbb{R}^3 \quad (1.15)$$

It is possible to define the so-called Chern numbers to identify if a certain state has non trivial topological features or not. These numbers are defined as

$$C_n = -\frac{1}{2\pi} \int_{BZ} d\mathbf{k} \cdot \Omega_{\mathbf{k}}, \quad (1.16)$$

what makes them also gauge invariant.

1.6 Fukui-Hatsugai-Suzuki and Niu methods

Let's now introduce two methods that to calculate Berry curvature and their associated Chern numbers; we will apply and compare them in the next sections with the Dirac and the Harper-Hofstadter models. The first one is the Fukui-Hatsugai-Suzuki [6] algorithm. When you want to compute the Berry connection of the state $|n\rangle$, you need the bra $\langle n|$ to be in the same gauge than $|n\rangle$ so $A_{\mu}^n = \langle n | \partial_{\mu} | n \rangle$. This algorithm allows us to do all the computations in the same gauge and hence get gauge invariant quantities in the end, as the Berry curvature or the Chern numbers are supposed to be. Furthermore, the discretization of the Brillouin zone poses no problem at all. The trick is to use the quantity

$$U_{\mu}(k_{\ell}) \equiv \frac{\langle n(k_{\ell}) | n(k_{\ell} + \hat{\mu}) \rangle}{|\langle n(k_{\ell}) | n(k_{\ell} + \hat{\mu}) \rangle|} \quad \in U(1) \quad (1.17)$$

where $k_{\ell} = (k_{j_1}, k_{j_2})$, $k_{j_{\mu}} = \frac{2\pi j_{\mu}}{N_{\mu}}$ and $j_{\mu} = 1, \dots, N_{\mu} - 1$ ($\mu = 1, 2$). Thanks to U_{μ} , we can calculate the Berry curvature⁴

$$\tilde{F}_{12}(l_{\ell}) = \ln \left(\frac{U_1(k_{\ell}) U_2(k_{\ell} + \hat{1})}{U_1(k_{\ell} + \hat{2}) U_2(k_{\ell})} \right), \quad -\pi \leq \frac{1}{i} \tilde{F}_{12} \leq \pi, \quad (1.18)$$

that is automatically gauge invariant. Obtaining the Chern numbers from this is quite straightforward: we need to integrate over the whole Brillouin zone; this corresponds to sum over all the

³If χ is regular on the path \mathcal{C} but not on everywhere on \mathcal{S} , then

$$\oint_{\mathcal{C}} \nabla \chi_{\lambda^{(n)}} \cdot d\lambda = \chi_{\text{fin}}^{(n)} - \chi_{\text{init}}^{(n)} = 2\pi n.$$

The Stokes theorem couldn't be used.

⁴The \sim simply indicates that we are talking about a quantity obtained from the code.

values of k_ℓ :

$$\tilde{c}_n = \frac{1}{2\pi i} \sum_{\ell} \tilde{F}_{12}(k_\ell) \quad (1.19)$$

What is remarkable about all of this resides in the fact that you can choose any⁵ discretization of the magnetic Brillouin zone, you get $\tilde{c}_n \in \mathbb{Z}$.

The second method is the Niu formula [7] that consists to calculate the Berry curvature of the level n as

$$\Omega_{\mathbf{k}}^n = \frac{1}{i} \sum_{n' \neq n} \frac{\langle n | \partial_{k_x} H | n' \rangle \langle n' | \partial_{k_y} H | n \rangle - \langle n | \partial_{k_y} H | n' \rangle \langle n' | \partial_{k_x} H | n \rangle}{(E_n - E_{n'})^2} \in \mathbb{R} \quad (1.20)$$

where $|n'\rangle$ is the eigenvector associated to $E_{n'}$. The demonstration of this formula consists to see that, for $n \neq n'$,

$$\begin{aligned} \langle n | \frac{\partial H}{\partial k_x} | n' \rangle &= \frac{\partial}{\partial k_x} (\langle n | H | n' \rangle) - \langle \frac{\partial n}{\partial k_x} | H | n' \rangle \\ &= \frac{\partial}{\partial k_x} (\langle n | E_n | n' \rangle) - \langle \frac{\partial n}{\partial k_x} | E_{n'} | n' \rangle \\ &= \langle \frac{\partial}{\partial k_x} n | E_n | n' \rangle + \langle n | \frac{\partial E_n}{\partial k_x} | n' \rangle - \langle \frac{\partial n}{\partial k_x} | E_{n'} | n' \rangle \\ &= (E_n - E_{n'}) \langle \frac{\partial n}{\partial k_x} | n' \rangle \end{aligned} \quad (1.21)$$

where we use $\langle n | n' \rangle = \delta_{nn'}$. By replacing this result in 1.15 (and following the same steps for k_y), we end up with 1.20.

2 Dirac and Honeycomb models

As a first model, let's take a simple one: the Dirac model [8]. We will inspect the spectrum then apply FHS and Niu methods to calculate the Berry curvature. We will briefly describe what Dirac cones and Dirac points are, when we close the gap between the bands of the spectrum. We finally compare the curvatures of Dirac model to the one of the honeycomb model near a Dirac point.

2.1 Dirac model

The Hamiltonian of the Dirac model is

$$H_D = v_F \mathbf{k} \cdot \boldsymbol{\sigma} + \Delta \sigma_z \quad (2.1)$$

where v_F , chosen equal to 1.5 here, is the Fermi velocity, $\mathbf{k} = (k_x, k_y)$, $\boldsymbol{\sigma} = (\sigma_x, \sigma_y)$, and Δ is the mass⁶ of the Dirac fermion. The spectrum corresponds to a two-states model whose spectrum

⁵Almost, see FHS paper

⁶The mass m will be equal to 0.05 all along this section.

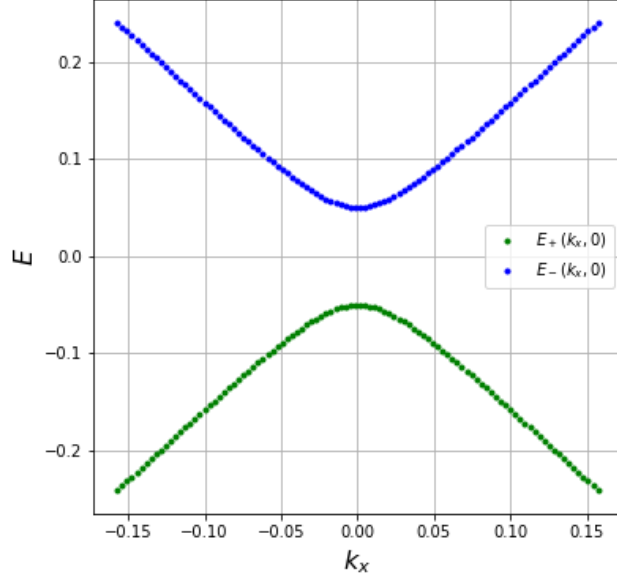


Figure 2: Spectrum of the Dirac model. Not all the Brillouin zone is taken into account since the most interesting part is near the point where the two bands are the closer to each other. This graph corresponds to $\Delta = 0.05$. If $\Delta = 0$, the two branches touch each other at $(0, 0)$.

is

$$E = \pm \sqrt{v_F^2 k^2 + \Delta^2} \quad \text{with} \quad k = \sqrt{k_x^2 + k_y^2} \quad (2.2)$$

as shown on the figure 2. When we put $\Delta = 0$, we observe a connection between the two bands at points called *Dirac points*. We call its hourglass structure a *Dirac cone*. The z -component of Berry curvature can be calculated for this model by the Niu formula or with the definition 1.15:

$$\Omega_z^\pm(k_x, k_y, \Delta) = \mp \frac{1}{2} \frac{v_F^2}{\sqrt{v_F^2 k^2 + \Delta^2}^3} \quad (2.3)$$

As this is visible on the figure 4, there is a ideal match with the FHS algorithm and the analytical result.

2.2 Honeycomb model

The Fourier transform of the Hamiltonian of the Honeycomb model is

$$\tilde{H}_{HC}(k_x, k_y) = \begin{pmatrix} \Delta & \sum_{i=1}^3 t_i e^{i\mathbf{k} \cdot \mathbf{d}_i} \\ \sum_{i=1}^3 t_i e^{-i\mathbf{k} \cdot \mathbf{d}_i} & -\Delta \end{pmatrix}. \quad (2.4)$$

where Δ is similar to a mass and the t_i 's are the hoppings along the \mathbf{d}_i vectors bonds between the

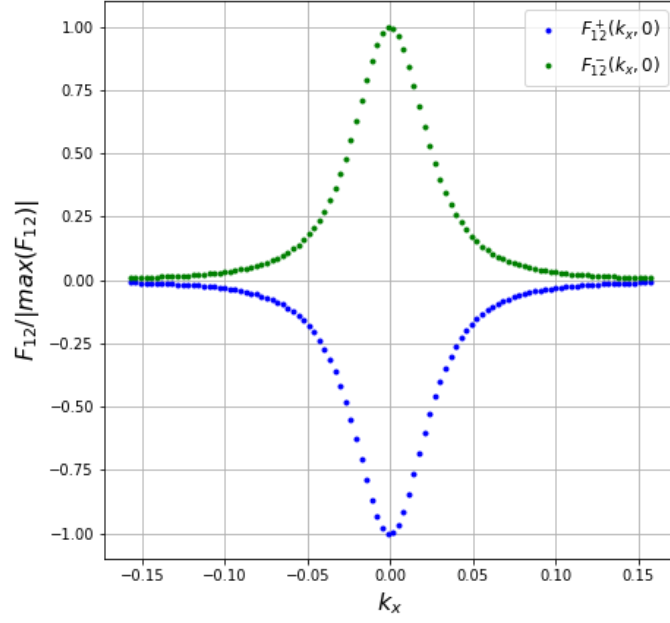


Figure 3: Curvatures F_{12}^+ and F_{12}^- computed with the FHS algorithm corresponding respectively to the bands E_+ and E_- .

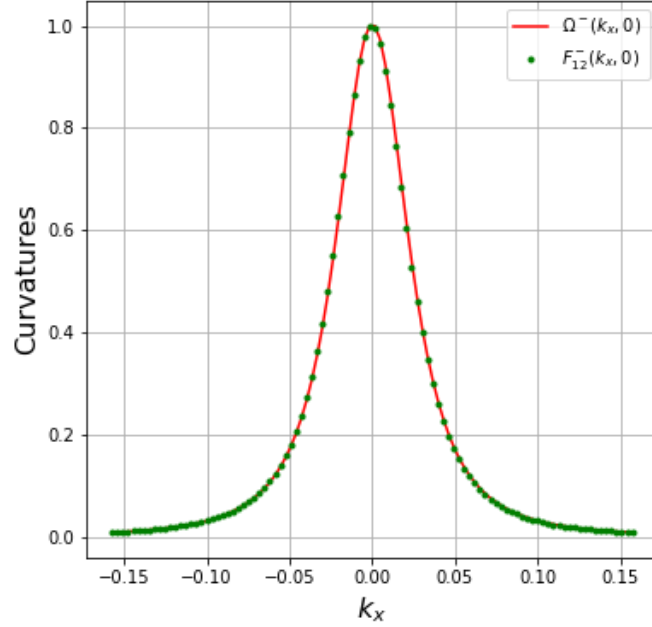


Figure 4: Comparison of the Berry curvature associated with the band E_- calculated with Niu formula (Ω^-) and FHS algorithm (F_{12}^-). The curvatures are divided by their maximum on the plot.

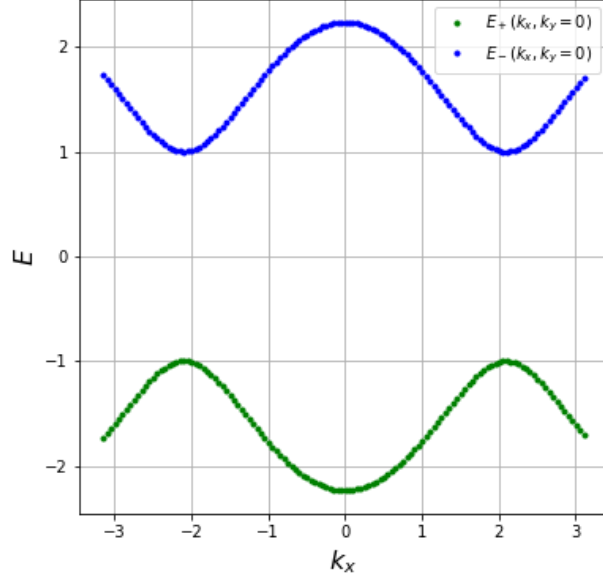


Figure 5: Spectrum of the Honeycomb model for $t_x = t_y = 1$ and $\Delta = 1$.

nearest neighbors:

$$\mathbf{d}_1 = \frac{a}{2}(1, \sqrt{3}), \quad \mathbf{d}_2 = \frac{a}{2}(1, -\sqrt{3}), \quad \mathbf{d}_3 = a(-1, 0) \quad (2.5)$$

where a is the real lattice parameter – here, $a = 1$. The spectrum of this Hamiltonian is presented on the figure 5. We remark the two Dirac cones at

$$\mathbf{K} = \frac{2\pi}{3a} \left(1, \frac{1}{\sqrt{3}} \right) \quad \mathbf{K}' = \frac{2\pi}{3a} \left(-1, \frac{1}{\sqrt{3}} \right) \quad (2.6)$$

For $\Delta = 0$, if we develop the formula of the Berry curvature for Honeycomb model around a Dirac point presented on the figure 6, you end up with the formula of Dirac model

$$\Omega_z^\pm(k_x, k_y, K_x, K_y, \Delta) = \mp \frac{1}{2} \frac{v_F^2}{\sqrt{v_F^2(\mathbf{k} - \mathbf{K})^2}}^3 \quad (2.7)$$

This can be checked on the figure 7 that compares these two model around \mathbf{K} . We note a correct match between the two graphs.

3 Harper-Hofstadter model ($\phi = 1/3$)

We now turn on a magnetic field. We review a few modifications to the Brillouin zone. We then explore a specific example of the Harper-Hofstadter model whose conditions are varied on the edges.

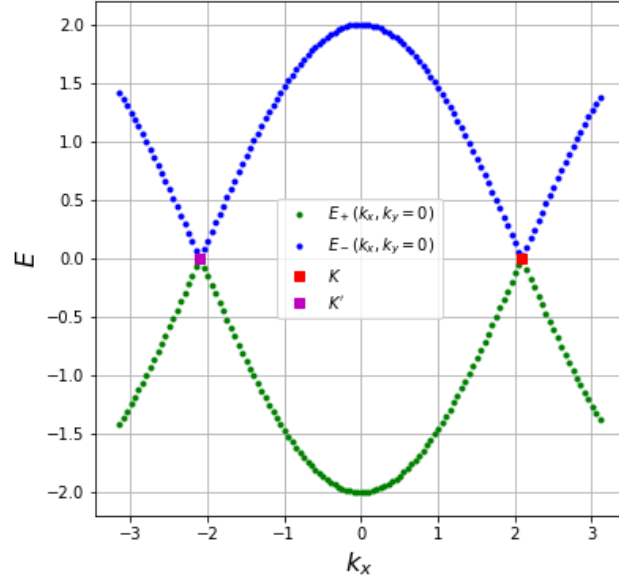


Figure 6: Spectrum of the Honeycomb model for $t_x = t_y = 1$ and $\Delta = 0$. We notice two Dirac points at $\mathbf{K} = \frac{2\pi}{3a} \left(1, \frac{1}{\sqrt{3}}\right)$ and $\mathbf{K}' = \frac{2\pi}{3a} \left(-1, \frac{1}{\sqrt{3}}\right)$.

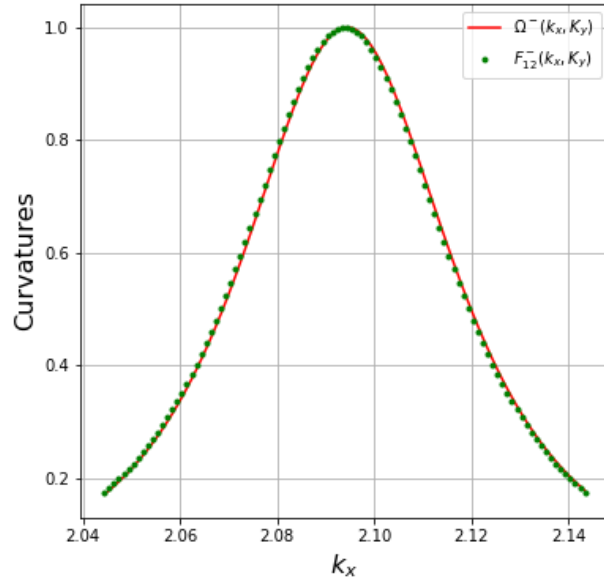


Figure 7: Comparison of the Berry curvature associated with the band E_- calculated with Niu formula 2.7 (Ω^-) for the Dirac model and FHS algorithm (F_{12}^-) applied to the honeycomb model. The curvatures are divided by their maximum.

3.1 Bloch states and magnetic Brillouin zone

Let's take electrons without interaction between them in a periodic potential that forms a rectangular lattice in two dimensions, where the real lattice parameters are a and b in the x and y directions respectively. We imposed a periodicity: the border $x = 0$ is identified with the border $x = L_x$ border and the same for $y = 0$ and $y = L_y$ border. Thus, the system is invariant under discrete translations⁷ \hat{T}_a, \hat{T}_b along the x and y directions respectively, so we get $[\hat{H}, \hat{T}_a] = [\hat{H}, \hat{T}_b] = [\hat{T}_a, \hat{T}_b] = 0$. The actions of \hat{T}_a and \hat{T}_b on a eigenstate $\psi(x, y)$ of \hat{H} are

$$\hat{T}_a \psi(x, y) = \psi(x - a, y) \quad \hat{T}_b \psi(x, y) = \psi(x, y - b). \quad (3.1)$$

By the commutation relations, we can find a common basis of eigenstates for \hat{H}, \hat{T}_a et \hat{T}_b . Since \hat{T}_a and \hat{T}_b are unitary, their eigenvalues are phase factors $e^{i\alpha}, \alpha \in \mathbb{R}$. So, if $\psi_{n,\mathbf{k}}$ is one of the eigenvectors, for n band energy index, then

$$\begin{aligned} \hat{T}_a \psi_{n,\mathbf{k}}(\mathbf{x}) &= e^{ik_x a} \psi_{n,\mathbf{k}}(\mathbf{x}) = \psi_{n,\mathbf{k}}(x - a, y), \\ \hat{T}_b \psi_{n,\mathbf{k}}(\mathbf{x}) &= e^{ik_y b} \psi_{n,\mathbf{k}}(\mathbf{x}) = \psi_{n,\mathbf{k}}(x, y - b), \end{aligned} \quad (3.2)$$

for $\mathbf{k} \in \mathbb{R}^2$. This suggests that $\psi_{n,\mathbf{k}} = e^{i\mathbf{k} \cdot \mathbf{x}} u_{n,\mathbf{k}}(\mathbf{x})$ où $u_{n,\mathbf{k}}(\mathbf{x}) = u_{n,\mathbf{k}}(x - a, y) = u_{n,\mathbf{k}}(x, y - b)$. A state in this form is called a *Bloch state*. Furthermore, we note that by changing $k_x \rightarrow k_x + \frac{2\pi}{a}$ et $k_y \rightarrow k_y + \frac{2\pi}{b}$, the Bloch state remains the same. It is therefore convenient to limit our analysis to $k_x \in (-\frac{\pi}{a}, \frac{\pi}{a}]$ and $k_y \in (-\frac{\pi}{b}, \frac{\pi}{b}]$.

From now on, let's introduce hopping factors t_x and t_y between sites of the lattice in the x and y directions respectively, and let's make a tight-binding approximation⁸, which means that the position eigenstates $|\mathbf{x}\rangle$ are restricted to the lattice sites $\mathbf{x} = (am, bn), m, n \in \mathbb{Z}$. The Hamiltonian is then given by

$$\hat{H} = -t_x \sum_{x,y} |x, y\rangle \langle x, y| - t_y \sum_{x,y} |x + a\hat{1}_x, y\rangle \langle x, y + b\hat{1}_y| + h.c. \quad (3.3)$$

Let's turn on now a uniform magnetic field $\mathbf{B} = B\hat{1}_z$, perpendicular to the lattice. The Hamiltonian $H_{\text{cont.}}$ is then modified since the vector field \mathbf{A} – whose rotational is the magnetic field – appears in it. If we didn't consider tight-binding, we would indeed have

$$\hat{H} = \frac{1}{2m} (\mathbf{p} + e\mathbf{A})^2, \quad (3.4)$$

where \mathbf{p} is the canonical momentum. By defining $\boldsymbol{\pi} = \mathbf{p} + e\mathbf{A}$, we see that $[\pi_x, \pi_y] = -ie\hbar B$. For $\hat{T}'_a = e^{i\hat{\pi}_x a}$ and $\hat{T}'_b = e^{i\hat{\pi}_y b}$, we see that

$$\hat{T}'_a \hat{T}'_b = \hat{T}'_b \hat{T}'_a e^{ieBab/\hbar}, \quad (3.5)$$

⁷These operators of translation are unitary and are generated by the impulsion operator in their respective direction: $\hat{T}_a = e^{i\hat{P}_x a}$ et $\hat{T}_b = e^{i\hat{P}_y b}$

⁸The particle can only jump from one site to the nearest neighbours. This jump can be seen as a tunnel effect

so \hat{T}'_a and \hat{T}'_b don't generally commute. Nevertheless, if you impose a magnetic flux through any plaquette such that $Bab = \Phi = n2\pi\hbar/e$ ($n \in \mathbb{Z}$), they commute again. If you reintroduce tight-binding with the previous notations, we get

$$\hat{H} = -t_x \sum_{x,y} |x,y\rangle e^{-ieaA_x(\mathbf{x})/\hbar} \langle x+a\hat{1}_x, y| - t_y \sum_{x,y} |x,y\rangle e^{-iebA_y(\mathbf{y})/\hbar} \langle x, y+b\hat{1}_y| + h.c. \quad (3.6)$$

By redefining \hat{T}_x and \hat{T}_y as

$$\begin{aligned} \hat{T}_x &= \sum_{x,y} |x,y\rangle e^{-ieaA_x(\mathbf{x})/\hbar} \langle x+a\hat{1}_x, y|, \\ \hat{T}_y &= \sum_{x,y} |x,y\rangle e^{-iebA_y(\mathbf{y})/\hbar} \langle x, y+b\hat{1}_y|, \end{aligned} \quad (3.7)$$

it gives

$$\hat{H} = -t_x (\hat{T}_x + \hat{T}_x^\dagger) - t_y (\hat{T}_y + \hat{T}_y^\dagger). \quad (3.8)$$

Moreover, the relation 3.5 still holds but we can actually go further. When the flux is a rational multiple of $\Phi_0 = 2\pi\hbar/e$, i.e. $\Phi = \frac{p}{q}\Phi_0$ with p and q integers which share no common divisor, we can build commuting operators by

$$[\hat{T}_x^{n_1}, \hat{T}_y^{n_2}] = 0 \quad \text{whenever} \quad \frac{p}{q}n_1n_2 \in \mathbb{Z} \quad (3.9)$$

This means that we can once again label the energy eigenstates by their eigenvalue under \hat{T}_y and, simultaneously, their eigenvalue under \hat{T}_x^q (if you pick $n_1 = q, n_2 = 1$ for example). They are Bloch-like eigenstates, satisfying

$$\hat{H} |\mathbf{k}\rangle = E(\mathbf{k}) |\mathbf{k}\rangle \quad \text{with} \quad \hat{T}_x^q |\mathbf{k}\rangle = e^{iqk_x a} |\mathbf{k}\rangle \quad \text{and} \quad \hat{T}_y |\mathbf{k}\rangle = e^{ik_y b} |\mathbf{k}\rangle \quad (3.10)$$

The important consequence of this is the modification of the Brillouin zone. We actually see the $e^{ik_x q a}$ is still periodic but with a $\frac{2\pi}{q}$ period. This modified Brillouin zone is called the *magnetic Brillouin zone*:

$$k_x \in \left[-\frac{\pi}{q}, \frac{\pi}{q}\right] \quad k_y \in [-\pi, \pi] \quad (3.11)$$

Its area is q times smaller than the usual Brillouin zone. In the following, we assume that $a = b = 1$. In addition, we opt for the gauge $\mathbf{A} = (0, \frac{p}{q}2\pi x, 0)$. The Hamiltonian then becomes⁹,

$$\hat{H} = -t_x \sum_{m,n} |m+1, n\rangle \langle m, n| - t_y \sum_{m,n} |m, n+1\rangle e^{2\pi m i \frac{p}{q}} \langle m, n| + h.c. \quad (3.12)$$

Before going to the Harper-Hofstadter model, let's focus on a little modification in the calculation of the Chern numbers, what has an influence on the conductivity. It is possible to deduce the conductivity of a state from its associated Berry curvature. We can indeed start from the Kubo

⁹Note the discretization of the space $(x, y) \rightarrow (m, n)$.

formula for conductivity of the r^{th} eigenstate, and after some simplifications – specific to our discussions – we get

$$\sigma_{yx}^r = ie^2 \sum_{\alpha=0}^r \int_{BZ} \frac{d^2k}{(2\pi)^2} (\langle \partial_{k_y} u_{\mathbf{k}}^\alpha | \partial_{k_x} u_{\mathbf{k}}^\alpha \rangle - \langle \partial_{k_x} u_{\mathbf{k}}^\alpha | \partial_{k_y} u_{\mathbf{k}}^\alpha \rangle), \quad (3.13)$$

where the sum is over the first r energy eigenstates (we start from the lowest energy). As required by the quantum Hall effect, σ_{yx} must be quantized. This reveals the topological nature of this effect. Actually, by changing a little the definition of the Chern numbers for system with magnetic field, we find that, for $\alpha = 1, \dots, q$:

$$C_\alpha = \frac{1}{2\pi} \int_{MBZ} d\mathbf{k} \cdot \boldsymbol{\Omega}_\alpha^\alpha \in \mathbb{Z} \quad (3.14)$$

so we finally obtain the so called TKNN formula

$$\sigma_{yx}^r = -\frac{e^2}{2\pi} \sum_{\alpha=0}^r C_\alpha. \quad (3.15)$$

We also adjust the Fukui-Hatsugai-Suzuki algorithm to this model. We now have $k_\ell = (k_{j_1}, k_{j_2})$, $k_{j_\mu} = \frac{2\pi j_\mu}{q_\mu N_\mu}$ and $j_\mu = 1, \dots, N_\mu - 1$ ($\mu = 1, 2$). Thus, these coordinates k_ℓ represent the magnetic Brillouin zone since q_μ is the denominator of the fraction of the magnetic flux ¹⁰ you introduce in the system (perpendicularly to the lattice). For the rest, it is the same story: we can similarly compute \tilde{F}_{12} and the Chern numbers, just by paying attention that the sum (discrete integration) is done on the magnetic Brillouin zone.

3.2 Toroidal boundary conditions

Let's maintain periodic boundary conditions on a finite square lattice whose length and width are L_x , in the x direction, and L_y , in the y direction. It is relevant to Fourier transform the Hamiltonian 3.12 in both directions since k_x and k_y are good quantum numbers. This leads to

$$\hat{H} = \bigotimes_{k_x, k_y} e^{i\mathbf{k} \cdot \mathbf{x}} \tilde{H}(k_x, k_y) e^{-i\mathbf{k} \cdot \mathbf{x}} \quad (3.16)$$

¹⁰We could have chosen a gauge where $q_1 = p$ and $q_2 = q$ are different from 1; a few lines above, we have chosen $q_1 = 1$ and $q_2 = q \in \mathbb{N}_0$.

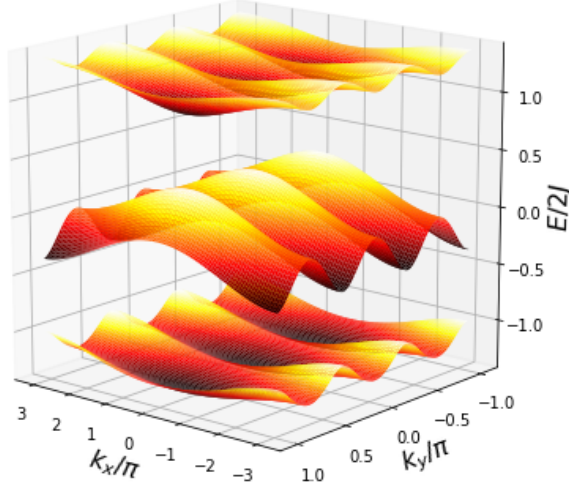


Figure 8: Spectrum of the Hamiltonian 3.17 (toroidal boundary conditions) on the magnetic Brillouin zone.

where

$$\tilde{H}(k_x, k_y) = \begin{pmatrix} -t_x 2 \cos(k_x) & 1 & 0 & \dots & e^{iqk_y} \\ 1 & -t_x 2 \cos(k_x + \frac{\pi}{2}) & 1 & \dots & 0 \\ 0 & \ddots & \ddots & \ddots & \vdots \\ \vdots & \vdots & \ddots & \ddots & 1 \\ e^{-iqk_y} & 0 & \dots & 1 & -t_x 2 \cos(k_x + \frac{(q-1)\pi}{2}) \end{pmatrix} \quad (3.17)$$

is called the Bloch Hamiltonian. In our case, and it will be the same for the rest of this work, we chose $p = 1, q = 3$. The spectrum, presented on the figure 8, exhibits a multilayer structure and, obviously, we find as many layers than the size of \tilde{H} , that is q layers as predicted by the Landau levels theory.

By using the FHS algorithm, we're able to calculate the Berry curvature F associated to each band for every couple (k_x, k_y) . We compared these results plotted on the figure 9 to the ones obtained with another method called the Niu's method. We can see there is no perfect match between the two results. Note that the local curvature obtained from the Niu's formula, Ω , is analytical whilst the local curvature got from FHS method, F , is dependent on the accuracy of

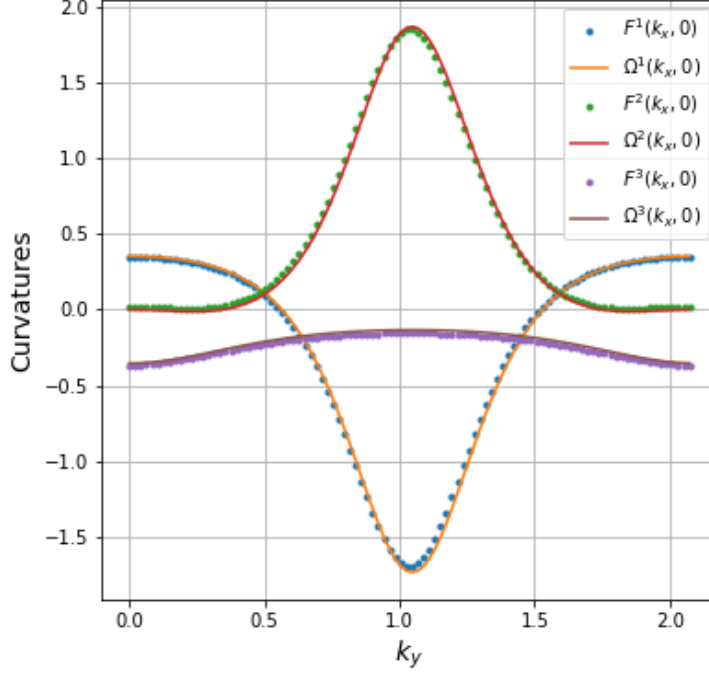


Figure 9: Comparison of Berry curvature obtained with Niu's method (Ω) and FHS algorithm F for $l = 1, 2, 3$ corresponding to the three bands of the spectrum ($q = 3$).

the algorithm since you need one plaquette of the Brillouin zone, whose the size depend on the discretization, to evaluate it in one point. Unfortunately, as it can be seen on the figure 10, the difference between these two doesn't converge to 0 but to a finite value. I couldn't solve this in the allotted time. The Chern numbers corresponding with each band are $-1, 2, -1$ (2 is for the one in the middle). The fact they don't vanish means we are facing a topological state of matter.

3.3 Cylindrical boundary conditions

We remove the periodicity only in the x direction. This means that we get a junction vacuum-sample on two sides of the sample. Thus, we apply the Fourier transform only in the y direction and get, for $\phi = p/q$,

$$\begin{aligned}
 \hat{H} &= -t_x \sum_{m, k_y} |m+1, k_y\rangle \langle m, k_y| - t_y \sum_{m, k_y} |m, k_y\rangle e^{-ik_y + 2\pi m i \phi} \langle m, k_y| + h.c. \\
 &= -t_x \sum_{m, k_y} (|m+1, k_y\rangle \langle m, k_y| + h.c.) - 2t_y \sum_{m, k_y} |m, k_y\rangle \langle m, k_y| \cos(k_y - 2\pi m \phi) \quad (3.18) \\
 &= \sum_{k_y} \hat{H}(k_y)
 \end{aligned}$$

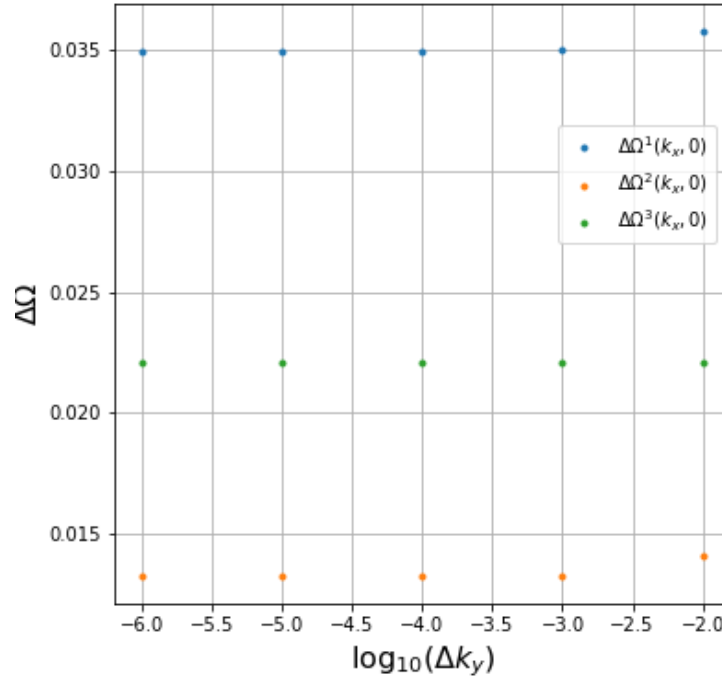


Figure 10: Absolute difference between curvature obtained with FHS algorithm (F^l) and the one calculated with Niu formula (Ω^l) ($l = 1, 2, 3$) for different discretization of the Brillouin zone.

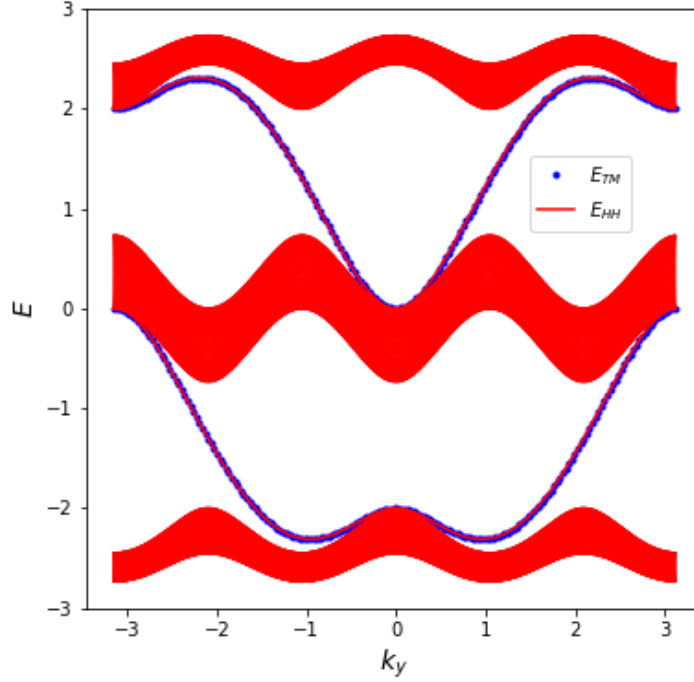


Figure 11: Spectrum E_{HH} for cylindrical boundary conditions for Hofstadter model 1/3, in red, compared with transfer matrix method E_{TM} in blue [9].

with $m = 0, \dots, L_x - 1$ and $k_y \in \left(-\frac{\pi}{q}, \frac{\pi}{q}\right]$. From this, we deduce that

$$\hat{H}(k_y) = \begin{pmatrix} -2t_y \cos(k_y) & -t_x & 0 & \dots & 0 \\ -t_x & -2t_y \cos(k_y - 2\pi\phi) & -t_x & \dots & 0 \\ \vdots & \vdots & \vdots & \ddots & -t_x \\ 0 & 0 & \dots & -t_x & -2t_y \cos(k_y - 2\pi\phi(L_x - 1)) \end{pmatrix} \quad (3.19)$$

This is apparently a 1-D problem along the x axis. To find the entire spectrum of \hat{H} , we can calculate the spectrum of $\hat{H}(k_y)$ for every k_y . We obtain a band structure presented on the figure 11. Moreover, we implemented the *Transfer Matrix Method*, introduced by Hatsugai that allows us to determine only the energy associated with the edge states. By superposing the edges states obtained with both methods, we see it fits properly¹¹ on figure 11.

Let's move on to edge states. When we pick a specific value of k_y , we get as many values of the energy as the number of sites along the x direction; we present this spectrum on figure 12. We clearly see that the two states associated to the two energies lying in the gaps are mostly localized

¹¹With a small modification to the code. Without this tiny trick, the graphs of the two methods don't match perfectly; I couldn't solve this either in the allotted time.

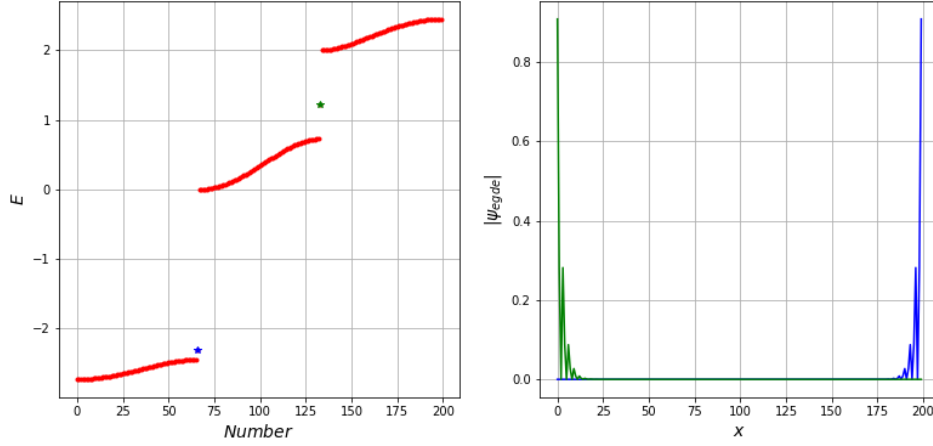


Figure 12: (Left) Spectrum for cylindrical boundary conditions for Hofstadter model 1/3 for $k_y = 1$. (Right) Absolute values of components of the states corresponding to energies in the gaps (little stars) presented on the left graph with correspondence colors.

on the edges of the sample.

3.4 Open boundary conditions

We now impose no periodicity at all. Our Hamiltonian, given by 3.12, is a $(L_x \times L_y) \times (L_x \times L_y)$ complex matrix

$H =$

$$\begin{pmatrix} -t_y \sum_n |0, n+1\rangle \langle 0, n| + h.c. & -t_x \sum_n |0, n\rangle \langle 1, n| + h.c. & 0 & \dots \\ -t_x \sum_n |1, n\rangle \langle 0, n| + h.c. & -t_y \sum_n e^{i2\pi\phi} |1, n+1\rangle \langle 1, n| + h.c. & -t_x \sum_n |1, n\rangle \langle 2, n| + h.c. & \dots \\ 0 & -t_x \sum_n |2, n\rangle \langle 1, n| + h.c. & \ddots & \ddots \\ \vdots & \ddots & \ddots & \ddots \end{pmatrix}$$

since we express the states of the system in the basis

$$\psi = \sum_{m,n} |m, n\rangle \langle m, n|.$$

Note that

$$-t_y e^{i2\pi\phi m} \sum_n |m, n+1\rangle \langle m, n| + h.c. = \begin{pmatrix} 0 & -t_y e^{i2\pi\phi m} & 0 & \dots \\ -t_y e^{-i2\pi\phi m} & 0 & -t_y e^{i2\pi\phi m} & \ddots \\ 0 & -t_y e^{-i2\pi\phi m} & 0 & \ddots \\ 0 & 0 & \ddots & \ddots \\ \vdots & \vdots & \vdots & \ddots \end{pmatrix}$$

and

$$-t_x \sum_n |m+1, n\rangle \langle m, n| + h.c. = \begin{pmatrix} -t_x & 0 & 0 & \dots \\ 0 & -t_x & 0 & \dots \\ \vdots & \ddots & \ddots & \ddots \end{pmatrix}$$

These two last matrices contain $L_y \times L_y$ complex elements and are obviously hermitian. We compute the eigenvalues of this system and present them on the figure 13. We notice this staircase structure that can be useful to detect the edge states. By selecting one eigenvalue in each gap, we can see that their associated state is actually mostly localized on the edges, as shown on the figure 14

4 Dynamics

To observe edge currents, we use the open boundary conditions system. We implemented two different initial states, a δ -function and an overlap with a Gaussian, and let them evolve in time. Concerning the δ -function, we choose to place an electron at coordinates (x_0, y_0) where the overlap between the δ -function and one of several edge states is the highest possible. We then plot the normalized state at different times and get the figure 15. We observe that the wavefunction splits into two pieces and propagates mostly along the edges. Nevertheless, we note the rapid decrease of intensity of the amplitude of the wavefunction and its dispersion into the bulk. The reason is that there is no eigenstate that is a perfect edge state in our case: there is always a non-vanishing amplitude in the bulk. In other words, if we could find such an eigenstate that is a perfect edge state with a non-vanishing amplitude only on the edge, the evolution would not disperse the wavefunction into the bulk since an eigenvector is preserved during evolution (if there is no degeneracy of the associated eigenvalue).

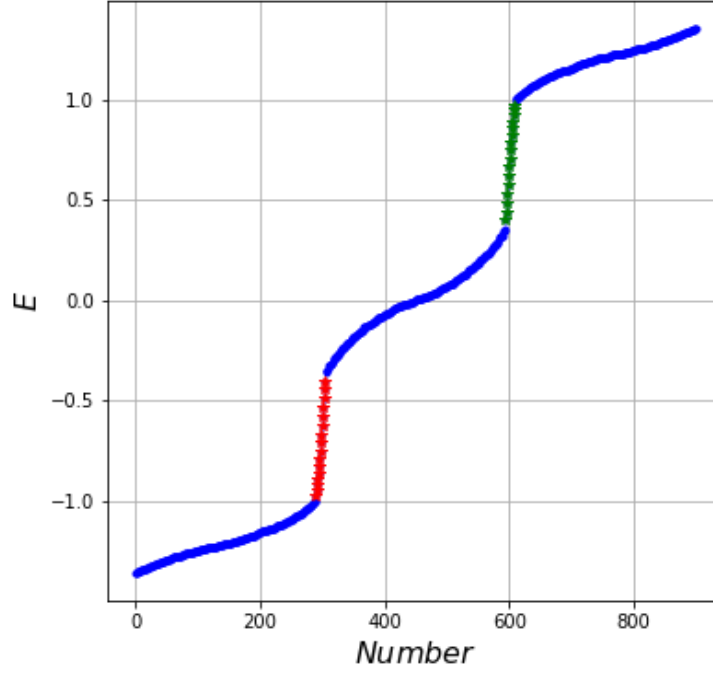


Figure 13: Spectrum of the Hamiltonian 3.12. The eigenvalues that are potentially associated to edge states are colored in red and green.

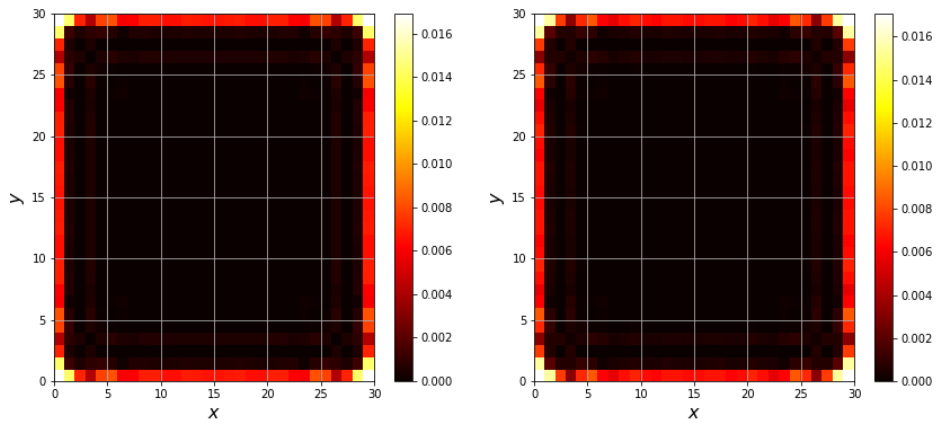


Figure 14: Two states corresponding to one eigenvalue in the lower gap (left) and one in the upper gap (right). They are mostly localized on the edges.

For a initial state that is an overlap between a Gaussian (that possesses a quasi-momentum k_y) and N edge states, more precisely

$$\begin{aligned}\psi(x, y, t = 0) &= \sum_{n=1}^N \left(\int dx' dy' \psi_n^*(x', y') \frac{1}{\sqrt{2\pi\sigma^2}} e^{-(y'-y_0)^2/2\sigma^2} e^{-ik_y y'} \right) \psi_n(x, y) \\ &\simeq \sum_{n=1}^N \left(\sum_{x', y'} \underbrace{\Delta x' \Delta y'}_{=1} \psi_n^*(x', y') \frac{1}{\sqrt{2\pi\sigma^2}} e^{-(y'-y_0)^2/2\sigma^2} e^{-ik_y y'} \right) \psi_n(x, y),\end{aligned}\tag{4.1}$$

we can observe two different results depending on the edge states you are summing on. Actually, regarding the spectrum on figure 13, you can sum over all of them or just select edge states corresponding to the energies in one of the two gaps. In the first case, you won't any qualitative difference to the precedent situation with the δ -function. The second one is more interesting: in function of the gap you selected, the wavepacket will go clockwise or counterclockwise, as you can see on figures 16 and 17. This is a consequence of the chirality of the system.

4.1 Comparison of velocities between cylindrical and open boundary systems

Let's remember that in the case the cylindrical boundary system, we chose to close the y -edges (L_y is assimilated to 0). Since there are only short range hoppings here, an electron cannot really detect whether it is in a cylindrical or in a open boundary system as long as it is in the middle of a y -edge (for L_y sufficiently large). This implies we can deduce several things from the cylinder case that apply to open case. For example, we may deduce the group velocity of the wavepacket in the open case, when it is propagating along a y -edge, thanks to the formula

$$v(k_y) = \frac{\partial E(k)}{\partial k}(k_y)\tag{4.2}$$

that is deducible in the cylindrical case. We warn the reader that we couldn't verify this affirmation due to a problem we couldn't solve in the allotted time. We still believe that the aforesaid comment about the similarities in both systems experienced by an electron in the middle of a y -edge, should lead to the wished result. If our code had correctly worked, here is the procedure we would have followed. First, you pick one value of k_y on the graph 11 in one of the two gaps. On one hand, we use it in the Gaussian function that we introduced in the equation 4.1 and we calculate the evolution of the overlap on the same gap as before along the y -edges; by that we mean you can track the position and extract the velocity of its motion, v_O . On the other hand, we evaluate v_C from the figure 11 using 4.2 for the same value of k_y . We expect that $v_C = v_O$.

4.2 Paper on photonics experiments

The reference [2] discusses an experiment on topological photonics systems based on the Hofstadter model. It is, roughly speaking, a question of replacing the electrons by photons but still experiencing the same results. To do so, the possibility of hopping between neighbor sites and a magnetic field are required. To understand how this can be engineered, we invite you to consult the

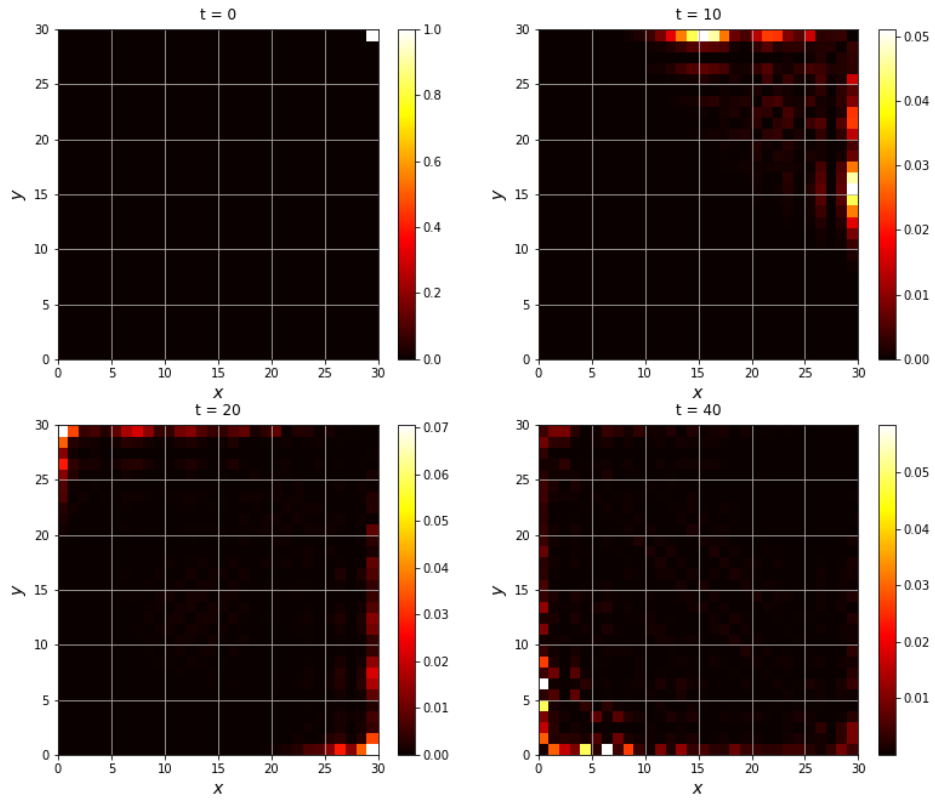


Figure 15: One electron is initially localized at site $(x_0, y_0) = (30, 30)$ as a δ -function at $t = 0$. At time $t > 0$, we see the splitting into wavepackets and the dispersion to the bulk and propagation along the edges.

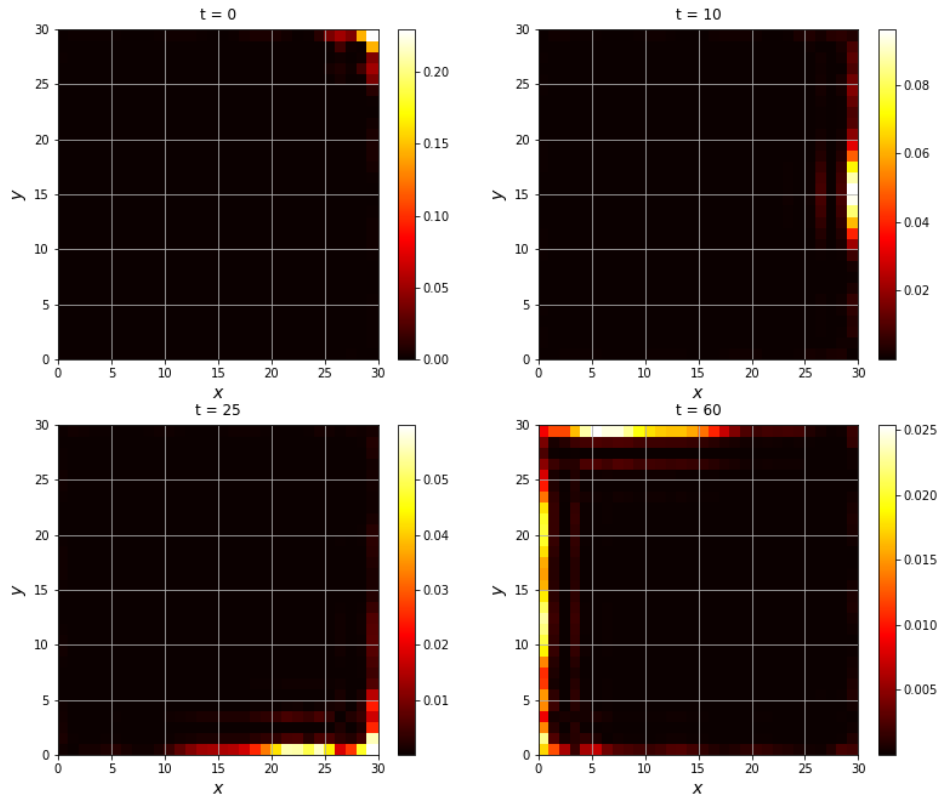


Figure 16: One electron is initially localized around site $(x_0, y_0) = (30, 30)$ as a Gaussian centered at $(x_0, y_0) = (30, 30)$ with $\sigma = 2$ at $t = 0$. At time $t > 0$, we see the wavepacket turning clockwise along the edges. Dispersion to the bulk is quasi invisible.

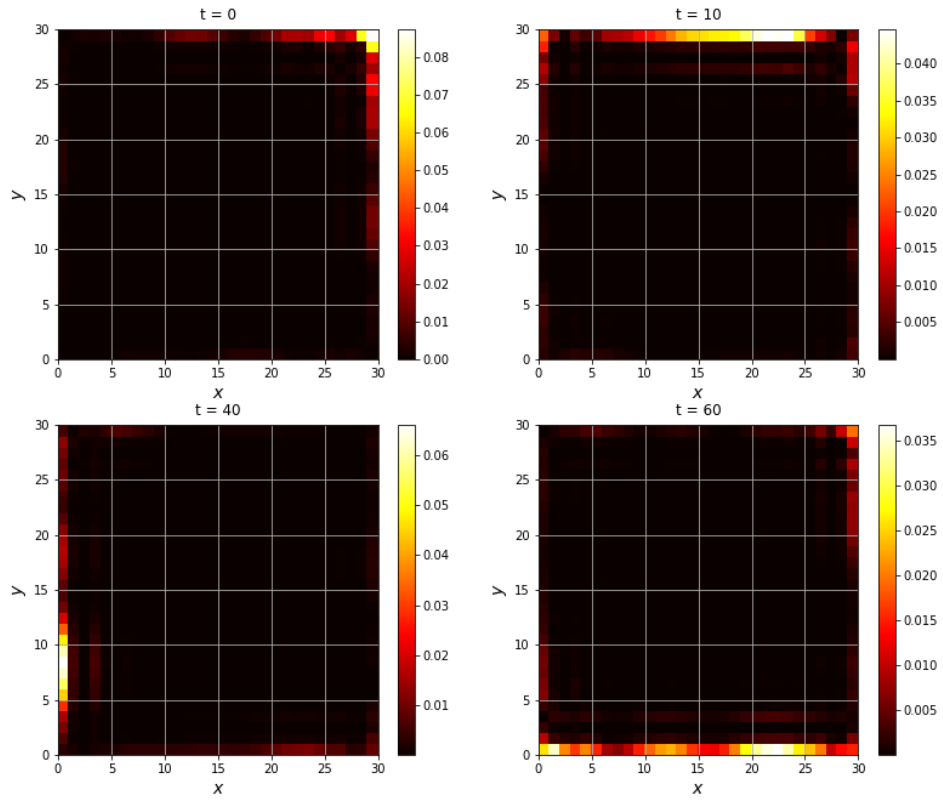


Figure 17: One electron is initially localized around site $(x_0, y_0) = (30, 30)$ as a Gaussian centered at $(x_0, y_0) = (30, 30)$ with $\sigma = 2$ at $t = 0$. At time $t > 0$, we see the wavepacket turning counterclockwise along the edges. Dispersion to the bulk is quasi invisible.

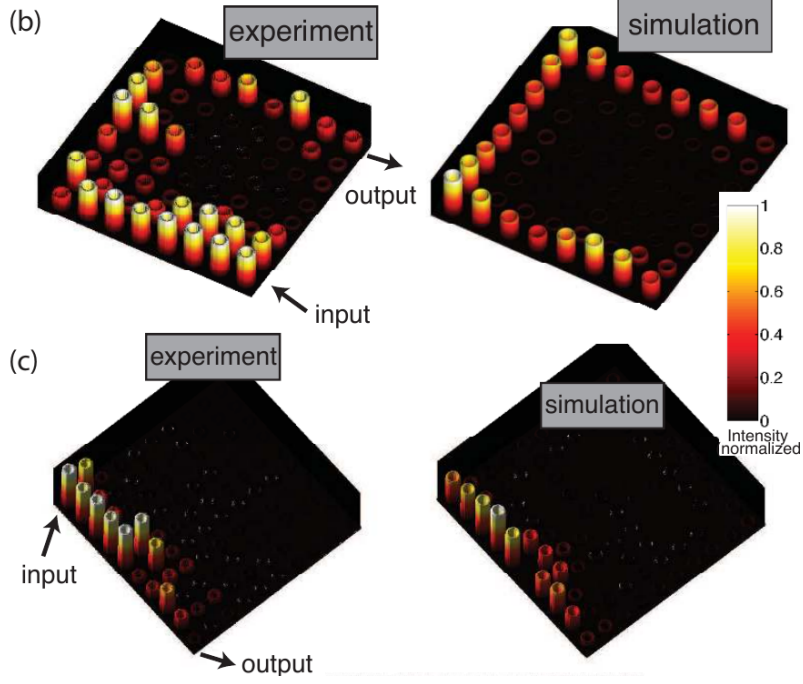


Figure 18: Image from the reference [2] (b) There is no resonator removed. Both the simulation and experiment exhibit chiral propagation on edges. (c) One resonator on the edge is removed. Both simulation and experiment show light routing around the missing resonator.

aforesaid reference. Although the experimental setup doesn't actually contain a real magnetic field element, a synthetic one can be created and thus influencing the photons hop between neighboring sites in two opposite directions, thanks to a specific arrangement of link and site resonators. As showed on the figure 18, topological edge states are observable experimentally. They are moreover chiral. The photons route around the missing resonator and then continue their path. By comparing this results from the paper with ours, we can argue they are qualitatively similar (not quantitatively). To observe they are "protected", one resonator can be removed from the path of an edge state. The light will simply route around the missing resonator.

5 Conclusions

After introducing the basic notions around topological physics and helpful to understand the quantum Hall effect, we compared the Berry curvature around a Dirac point for the Dirac and honeycomb systems. It appears they match arguably well.

Right after, we discussed the modifications that a magnetic field can imply on the system and particularly on the Brillouin zone. This allowed us to describe the 1/3 Hofstadter model with different boundary conditions.

We then let the system evolve for two different initial conditions. The overlap with the δ -function separated in two wavepackets that propagated in opposite directions, contrary to the Gaussian overlap, that took the path in a clockwise or a counterclockwise direction depending on the gap overlapped; this exhibited the chiral nature of a such system.

Eventually, we tried to verify the consistency of the models by comparing the behavior of an electron in the cylindrical and open systems near a y -border. While this is consistent in theory and we believe this can be proved, we didn't managed to it in this report. We finally confronted our results with the ones of a paper of topological photonics. Hafezi at al. actually ended up with the same conclusions concerning the propagation of the current along the edges.

References

- [1] DAVID TONG. Lectures on the Quantum Hall Effect. 2016. (see p. 2)
- [2] TOMOKI OZAWA, HANNAH M. PRICE, ALBERTO AMO, NATHAN GOLDMAN, MOHAMMAD HAFEZI, LING LU, MIKAEL RECHTSMAN, DAVID SCHUSTER, JONATHAN SIMON, ODED ZILBERBERG, **and** IACOPO CARUSOTTO. Topological Photonics. **91**: 2018. (see pp. 3, 21, 25)
- [3] JEAN DALIBARD. La matière topologique et son exploration avec les gaz quantiques. *Collège de France, chaire Atomes et rayonnement*, URL: https://www.college-de-france.fr/media/jean-dalibard/UPL7297697706384107935_Dalibard_notes3_20140528.pdf(see p. 3)
- [4] JEAN DALIBARD. La matière topologique et son exploration avec les gaz quantiques. *Collège de France, chaire Atomes et rayonnement*, URL: http://www.phys.ens.fr/~dalibard/CdF/2018/notes_cours_total.pdf(see p. 3)
- [5] JEAN DALIBARD. Introduction to the physics of artificial gauge fields. 2015. (see p. 3)
- [6] T. FUKUI, Y. HATSUGAI, **and** H. SUZUKI. Chern numbers in discretized Brillouin zone: Efficient method of computing (spin) Hall conductances. *Journal of the Physical Society of Japan*, **74**: 1674–1677, 2005. (see p. 5)
- [7] DI XIAO, MING-CHE CHANG, **and** QIAN NIU. Berry phase effect on electronic properties. *Reviews of Modern Physics*, **82**: 2010. (see p. 6)
- [8] B ANDREI BERNEVIG **and** TAYLOR L. HUGHES. Topological insulators and topological superconductors. *Topological Insulators and Topological Superconductors*, 2013. (see p. 6)
- [9] HATSUGAI. Edge states in the integer quantum Hall effect and the Riemann surface of the Bloch function. *Physical review. B, Condensed matter*, **48**: 1993. (see p. 17)